



HAL
open science

Galling categories investigations in stainless steels

T. Lesage, Salima Bouvier, A. Oudriss, Y. Chen, Marion Risbet, P.-E.
Mazeran

► **To cite this version:**

T. Lesage, Salima Bouvier, A. Oudriss, Y. Chen, Marion Risbet, et al.. Galling categories investigations in stainless steels. *Wear*, 2020, 460-461, pp.203413. 10.1016/j.wear.2020.203413 . hal-03180864

HAL Id: hal-03180864

<https://utc.hal.science/hal-03180864v1>

Submitted on 21 Sep 2022

HAL is a multi-disciplinary open access archive for the deposit and dissemination of scientific research documents, whether they are published or not. The documents may come from teaching and research institutions in France or abroad, or from public or private research centers.

L'archive ouverte pluridisciplinaire **HAL**, est destinée au dépôt et à la diffusion de documents scientifiques de niveau recherche, publiés ou non, émanant des établissements d'enseignement et de recherche français ou étrangers, des laboratoires publics ou privés.



Distributed under a Creative Commons Attribution - NonCommercial 4.0 International License

Galling categories investigations in stainless steels

T. Lesage^{1,*}, S. Bouvier¹, A. Oudriss², Y. Chen³, M. Risbet¹, P-E. Mazeran¹

¹ Sorbonne University, UTC, CNRS, FRE 2012 Roberval, France

² LaSIE, CNRS UMR 7356, Université de La Rochelle, La Rochelle, France

³ CETIM, Pôle matériaux métalliques et surfaces, Senlis, France

Corresponding author: thibault.lesage@railenium.eu – 180 Rue Joseph-Louis Lagrange, 59540 Valenciennes, France

Abstract

This paper focuses on the galling mechanisms occurring in stainless steels and aims to provide a better comprehension of the effects of microstructure on galling resistance. Five stainless steels are studied in this paper, namely Nitronic60, AISI660, 316L, 316LN (austenitic stainless steels) and Uranus45N (duplex austenite-ferrite). Both surface topography and in-depth microstructure are characterized in order to determine the consequences of galling apparition. Experimental investigations at macroscopic and microscopic scales show that galling can occur following several mechanisms. Galling leads to either adhesive wear spots randomly distributed on the surface (tolerant galling), adhesive wear initiated on the periphery of the pin (moderate galling) or abrasive wear and smearing (severe galling). Depending on these categories, the galling threshold and severity are highly variable. Studying these specific mechanisms can help us predict and eventually increase galling resistance for a given material couple. Thus, several microstructural investigations have been performed in order to discuss about the possible origins of these galling categories.

Keywords: Galling mechanisms, surface topography, microstructure, stainless steels

24 1. Introduction

25 Galling is a severe case of adhesive wear, defined by the ASTM committee G02 on wear and
26 erosion in Standard G40 [1] as "a form of surface damage arising between sliding solids,
27 distinguished by macroscopic, usually localized, roughening and creation of protrusions above
28 the original surface". Galling goes with the apparition of undesirable surface modifications,
29 leading to the deterioration of the materials in contact [2]. Galling is problematic for a wide
30 range of industrial applications, e.g. medical instruments, sheet metal forming, nuclear plants
31 [3]. In most of these industries, stainless steels are widely used due to their relative ease of
32 manufacture, high strength, stiffness and excellent corrosion resistance. However, stainless
33 steels are likely to develop galling [4,5], making galling resistance one of the key parameters in
34 determining tool lifetime in such industries [6]. Even though the use of lubricants can easily
35 lower the tendency to galling [7], lubrication could be undesirable *e.g.* in food-processing or
36 pharmaceutical industries, which explains the increasing interest in dry sliding conditions [8].
37 As a consequence, numerous studies focus on increasing galling resistance [9–11] of different
38 materials couples. Several factors are already known to increase the risk of galling, *e.g.* using
39 mating surfaces with similar chemical compositions and mechanical properties, working at
40 elevated temperature or using high load across interface [12]. Stacking fault energy (SFE) is one
41 of the key parameters controlling galling resistance [12,13]. The material having a high amount
42 of stacking fault energy are usually more vulnerable towards galling [14].

43 However, the influence of microstructure on galling resistance is still unclear. In the literature,
44 most of the work on the influence of microstructure on galling resistant is related to either
45 particle studies (carbides, nitrides...) or crystallographic phases. The effects of the size, spatial
46 distribution and hardness of carbides have been studied in several types of steels [8,15–17].
47 Homogeneous distribution of small size particles is believed to increase galling resistance while
48 bigger and inhomogeneously distributed particles lower galling resistance. The influence of
49 crystallographic phase on galling resistance has also been studied, in particular in cobalt-base
50 alloys or hard-facing alloys [18,19]. Most of the studies indicates that the galling tendency is

51 increased for phases having c/a ratio low *e.g.* cubic phases. Conversely, HCP structure having
52 an important c/a ratio are less prone to galling [14]. However, these studies on the impact of
53 microstructure on galling resistance are still seldom and it remains hard to have an overall view.
54 Moreover, one can notice that galling resistance is most often only defined by galling threshold
55 [20]. Even if some authors [21–23] have recently been trying to take galling severity into
56 account, very few data is still to be found in the literature. Additional efforts must be provided
57 to fully apprehend galling phenomenon and propose relevant mechanisms. Classical approach
58 using sole surface investigations has proven to be insufficient to propose trustworthy galling
59 mechanisms. The relationship between microstructure and galling resistance is only slightly
60 considered in the literature. This work combines surface observations and microstructure
61 investigations in order to better characterize galled samples and understand galling mechanisms.
62 To do so, this work is supported by a comparative study using various stainless steel grades.
63 The opposition between microstructural responses from identical galling tests has lead us to
64 propose novel galling categories. These categories will provide a better understanding of the
65 mechanisms behind galling phenomenon and eventually help preventing galling onset.

66 2. Materials and methods

67 Five stainless steels are selected in this study, namely 316L, 316LN, Nitronic60, AISI660
68 (austenitic stainless steels) and Uranus45N (duplex austenite-ferrite). These grades differ by
69 their chemical composition, crystallographic structure and mechanical properties, as presented
70 in Table 1 and Table 2. Most data are coming from ThyssenKrupp provider, while surface
71 hardness and grain size are determined experimentally. Surface hardness is determined by nano-
72 indentation using a Berkovich tip with an indentation depth of 1 μm and a peal hold time of 10
73 seconds. Grains size is measured by Electron BackScatter Diffraction (EBSD) realized on as-
74 received material.

75

Table 1 : Chemical composition in mass percent and crystallographic phase of the selected stainless steels

	C	Si	Mn	Ni	Cr	Mo	N	Other	Fe (eq)	Phase
Nitronic60	0.06	4.12	8.05	8.56	17.02	0.75	0.15	/	61.44	Austenite
AISI660	0.08	0.34	1.30	23.35	14.5	1.16	/	Ti 2.68	56.60	Austenite PH
Uranus45N	0.02	0.44	1.35	5.32	22.70	2.55	0.16	/	67.46	Austenite-ferrite
316L	0.02	0.58	1.30	10.08	16.90	2.03	0.04	/	69.05	Austenite
316LN	0.01	0.29	1.85	13.25	17.05	2.61	0.16	/	64.78	Austenite

76

77

Table 2 : Mechanical properties of the selected stainless steels. Surface hardness is determined by nanoindenting

78

tests realized on the surface and grain size is measured by EBSD investigations

	R _e (MPa)	R _m (MPa)	R _m /R _e	Elongation (%)	Surface hardness (GPa)	Grain size (μm)
Nitronic60	379	732	1.93	35	6.7 ± 1.1	126 ± 18
AISI660	635	995	1.57	35	8.5 ± 0.9	18 ± 7
Uranus45N	542	757	1.40	25	7.9 ± 0.7	14 ± 6
316L	293	555	1.89	35	6.1 ± 1.2	34 ± 10
316LN	296	626	2.11	17	6.6 ± 0.6	75 ± 15

79

80

Electron BackScatter Diffraction (EBSD) investigations are performed on as-received materials

81

as well as galled samples. Sample preparation for EBSD analysis is done by manual polishing

82

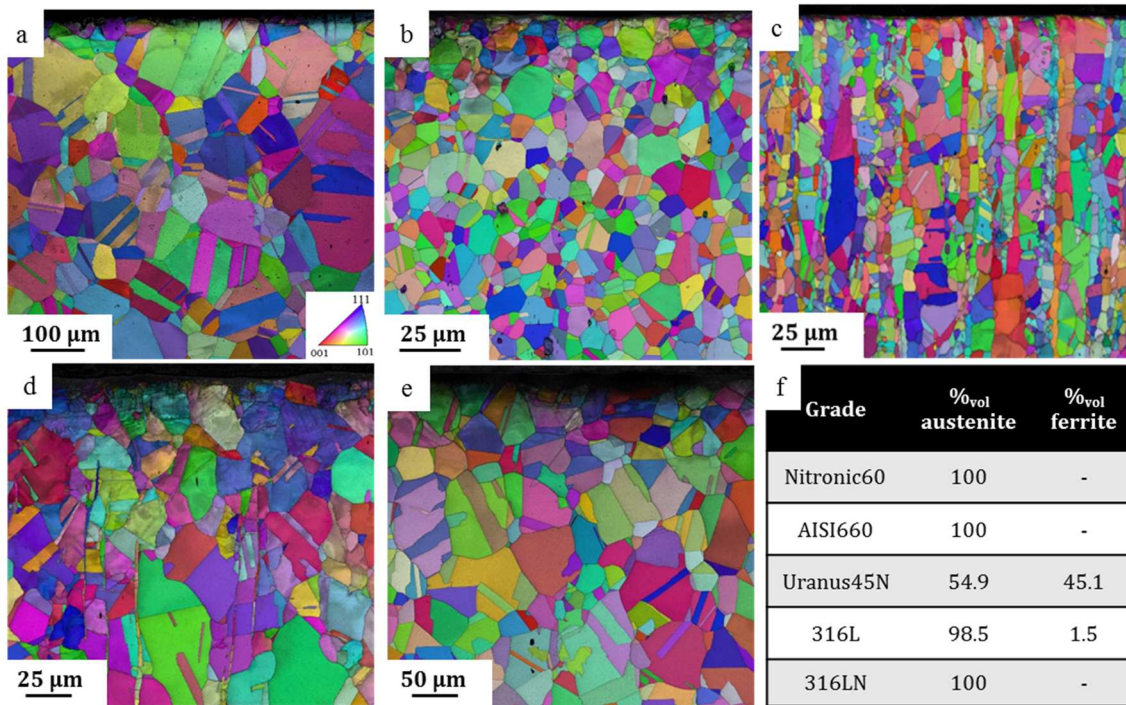
(grid papers up to 4000), followed by 3 μm and 1 μm diamond paste polishing. Finally,

83

vibration polishing is used with 50% OPS – 50% H₂O solution for 10 hours at 100% vibration

84

and 72 hours at 10% vibration. Resulting EBSD orientation maps are presented in Figure 1.



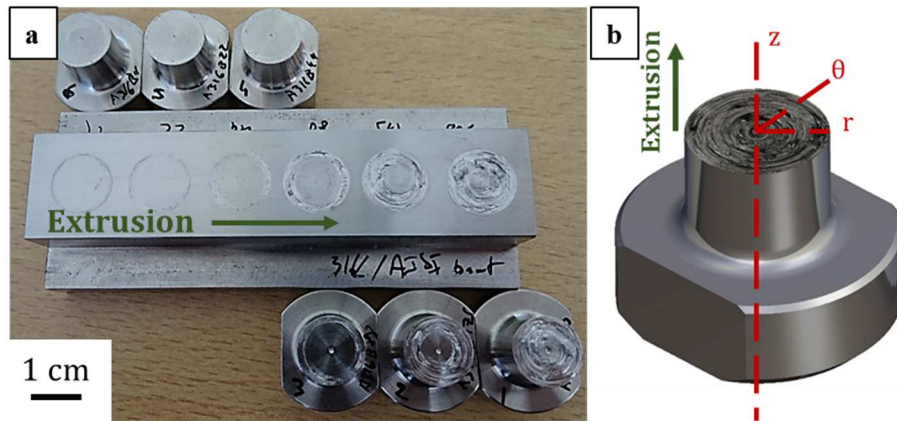
85

86 *Figure 1: Inverse pole figure (IPF) for the as-received materials. a- Nitronic60, b- AISI660, c- Uranus45N, d- 316L,*
 87 *e- 316LN and f- Austenite and ferrite percent for each grade*

88 Galling tests are performed following the ASTM G98 standard. It consists of a pin-on-bloc test
 89 where a $\varnothing 12.7$ mm pin rotates on a flat surface. The mating block is always made of 316L since
 90 this grade is one of the most used stainless steel in nuclear and pharmaceutical industries. Pins
 91 and blocks are directly machined from extruded bars as designed in ASTM G98 standard [2].
 92 All samples come from round bars which have been hot rolled and annealed peeled by the steel
 93 providers. All pins are then machined from as received bars in such a way that contact surface is
 94 following extrusion direction perpendicular to contact surface. As opposite, due to the important
 95 length of tested blocs, contact surface is set parallel to extrusion direction of the initial bar.

96 Figure 2.a shows the typical pins and plates morphology after galling test, while Figure 2.b
 97 represents the cylindrical coordinates system used.

98



99

100

Figure 2 : a- Pin and block samples after galling tests and b- cylindrical coordinates used for the pin

101

Since roughness and surface state are of great importance on galling resistance [4], initial Ra is

102

carefully controlled before galling test. Pins surface are turned while blocks are grinded, with an

103

initial Ra for both pins and plates of $0.30 \pm 0.04 \mu\text{m}$.

104

To realize the galling test itself, a tension compression Instron machine (capacity 250kN) is

105

used with a load cell A212-201 (250 kN) [2]. The pin is first subjected to a compressive force,

106

ranging from 8kN to 250kN depending on test condition. The pin is then slowly rotated (one

107

turn in six seconds) while maintaining the contact with the plate (Figure 3.a). One single

108

rotation (360°) is done and the occurrence or not of galling is determined by unassisted visual

109

observation. Galling occurrence is stated if any surface degradation is visible by this sole mean

110

[2]. Each pin is used only once, while blocs can be used for 6 consecutive galling tests, using

111

every time a virgin surface. Galling threshold is determined following a dichotomy tree, starting

112

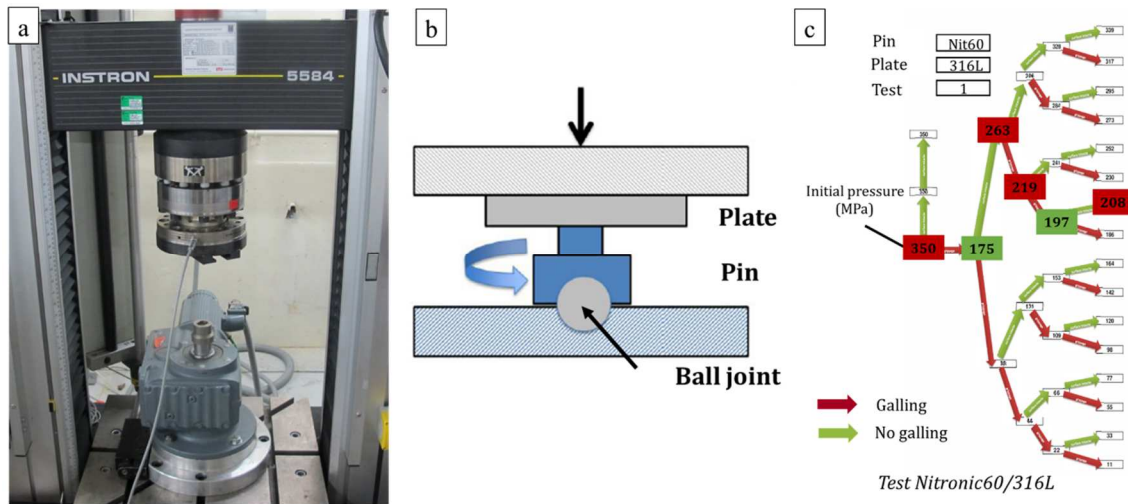
at a maximum pressure of 350 MPa and then decreased progressively, following the path

113

defined in Figure 3.b. Galling threshold is defined as the average between maximum pressure

114

without galling occurrence and minimum pressure with galling occurrence.



115

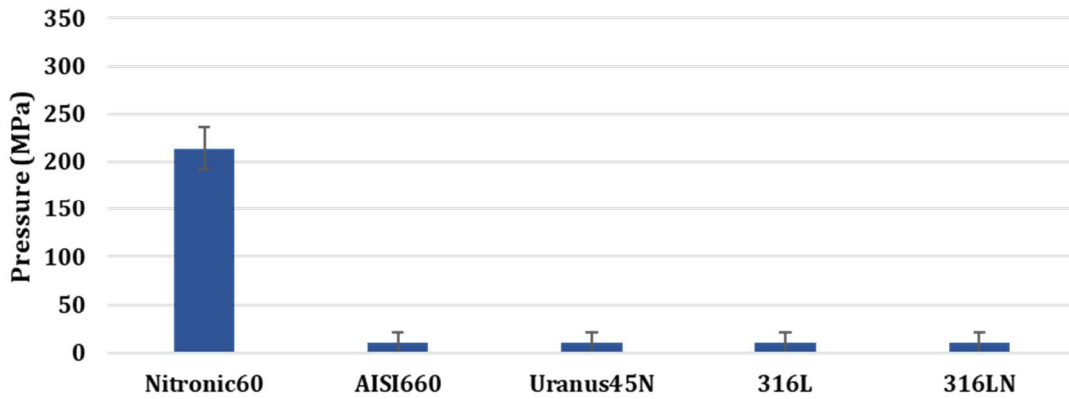
116 *Figure 3 : a- ASTM G98 experimental galling test setup, b- schematic of the set up used for ASTM G98 galling test*
 117 *and c- ASTM G98 galling test procedure taking as example a Nitronic60/316L test*

118 After galling test, the occurrence of galling is determined using ASTM G98 8.9 standard. This
 119 standard indicates that a sample is galled if any macroscopic surface modification apart from
 120 scoring and surface waviness is to be seen with unassisted visual observation. *In situ* acoustic
 121 emission measurements could confirm the occurrence of galling, as proposed in Saidoun *et al.*
 122 [24].

123 Surface topography measurement are performed by non-contact 3D profilometry Sensofar S
 124 Neox. Material transfer associated with galling is confirmed by Energy-Dispersive
 125 Spectroscopy (EDS) on both surfaces. Microscale observations are realized by Scanning
 126 Electron Microscopy (SEM) observation on Zeiss Sigma microscope, a current of 25kV is used
 127 for both imaging and EBSD mapping. The EBSD patterns acquisition are made with the
 128 software Nordif UF1100 and the corresponding mapping done by OIM Data collection 5.3.
 129 Local misorientation is determined via Kernel Average Misorientation (KAM) maps. Analyses
 130 are either realized following cross section observations (rz section Figure 2.b) or longitudinal
 131 observations (rθ section).

132 3. Galling categories investigations

133 Figure 4 displays the galling thresholds of each considered stainless steel grade tested against a
134 316L plate. Each test has been repeated three times for repeatability estimations.



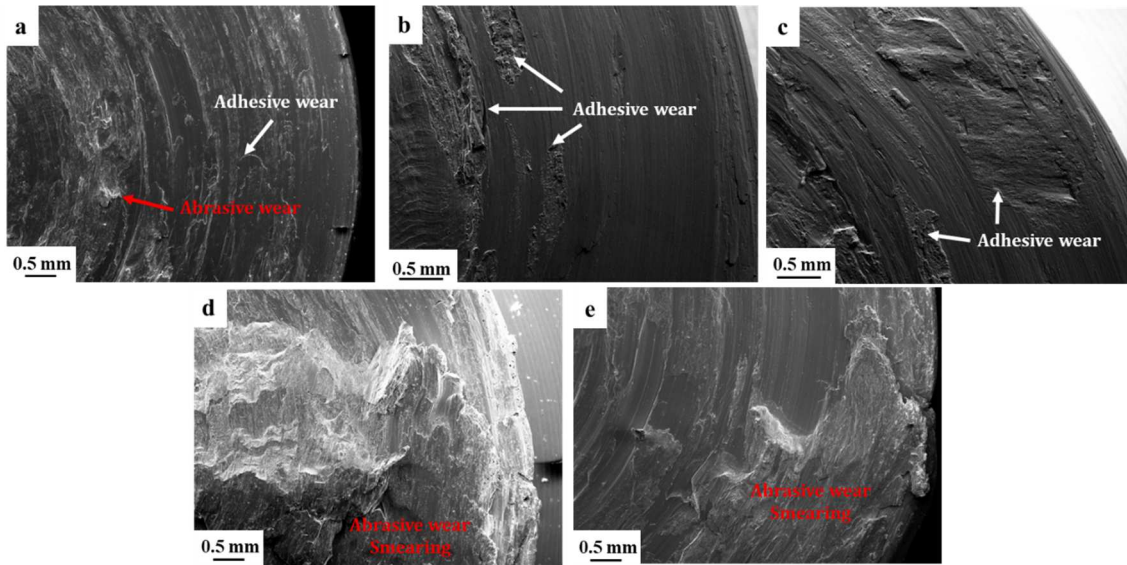
135

136 *Figure 4 : Galling threshold in ASTM G98 configuration for different grades of pins mated with a block of 316L*

137 Selected stainless steels exhibit very low galling threshold, lower than 11 MPa (minimum
138 pressure applicable for this test) except for Nitronic60, having a galling threshold of 214 ± 16
139 MPa. Considering only galling threshold, one could therefore consider that Nitronic60 presents
140 a high “galling resistance” while the other four grades all present an equivalent galling
141 resistance. However, as presented onwards, galling threshold is not sufficient to determine the
142 galling resistance and noticeable differences can be observed between these five grades.

143 3.1. Surface state investigations

144 Visual and SEM observations indicate that surface morphology differs from one material to
145 another, as shown on Figure 5.



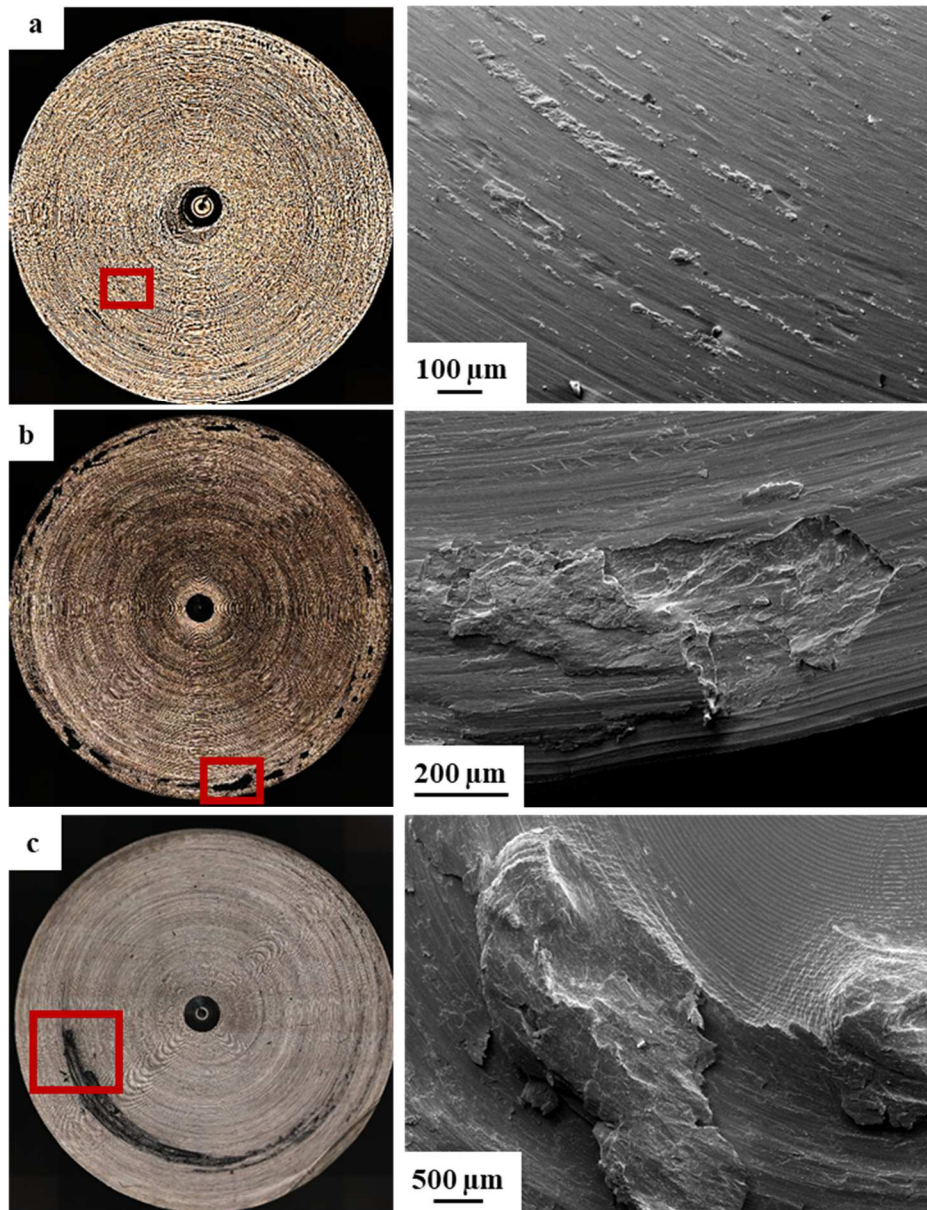
146

147 *Figure 5 : SEM observations at mesoscopic scale for samples after galling test at 350 MPa in the case of a-*

148 *Nitronic60, b- AISI660, c- Uranus45N, d- 316L, e- 316LN*

149 We observe after galling test at 350 MPa for Nitronic60 a combination of abrasive and adhesive
 150 wear of small dimension, leading to a qualitatively weakly degraded surface. AISI660 and
 151 Uranus45N exhibit mainly adhesive wear on the surface with the existence of material transfer,
 152 confirmed by EDS analysis. Finally, both 316L and 316LN present abrasive wear and smearing
 153 observed on the whole surface.

154 Nitronic60, AISI660 and 316L are the most representative grades for each wear phenomena and
 155 are therefore presented in more details. Figure 6 represents typical surfaces observed after
 156 galling test at contact pressure slightly higher than galling threshold.



157

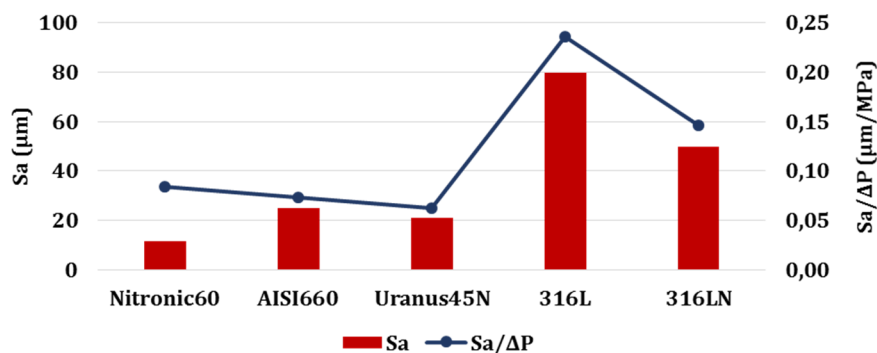
158 *Figure 6 : Macroscopic observation and SEM observations of the surface slightly higher than galling threshold for a-*
 159 *Nitronic60 at 224 MPa showing localized adhesive wear spots leading to galling initiation sites, b- AISI660 at 22*
 160 *MPa showing adhesive wear observed along the periphery of the pin and c- 316L at 22 MPa showing third body*
 161 *abrasive wear by smearing observed all over the surface*

162 Macroscopic observations show that Nitronic60 (Figure 6.a) presents a high number of localized
 163 adhesive wear spots homogenously distributed on the whole surface. Material transfer locally
 164 occurs at these points, as confirmed by EDS analysis. Almost no smearing or abrasive wear is
 165 observed at a pressure slightly higher than galling threshold. In the case of AISI660 (Figure 6.b)
 166 wear is mostly adhesive and localized on the periphery of the pin. Almost no wear is observed

167 outside the periphery of the pins. Very little abrasive wear can be found for this grade.
168 Ultimately, 316L (Figure 6.c) shows a high amount of third body abrasive wear and smearing,
169 even at low pressure. Smearing can be found randomly on the whole surface of the pin,
170 especially at higher pressure. Conversely to Nitronic60 and AISI660, adhesive wear is not likely
171 to be found.

172 These qualitative observations are completed with surface topography investigation (Figure 7).
173 Sa parameter is determined after a galling test realized at 350 MPa. In order to ensure
174 comparative data, measured Sa is then divided by the pressure difference ΔP between 350 MPa
175 and galling threshold ($\Delta P = 339$ MPa for all grades except for Nitronic60: $\Delta P = 136$ MPa). Sa
176 value accounts for the consequences of galling test for a given load while the reduced Sa/ ΔP is
177 representative of the consequences of galling for a given over-pressure subsequent to galling
178 threshold.

179 Measurements are realized on a quarter of the surface of the plate (7.5×6.5 mm²) to ensure
180 representative data.



181
182 *Figure 7 : Sa parameter measured after galling test realized at 350 MPa. Sa value is then divided by pressure*
183 *difference in order to have comparative values for different galling thresholds*

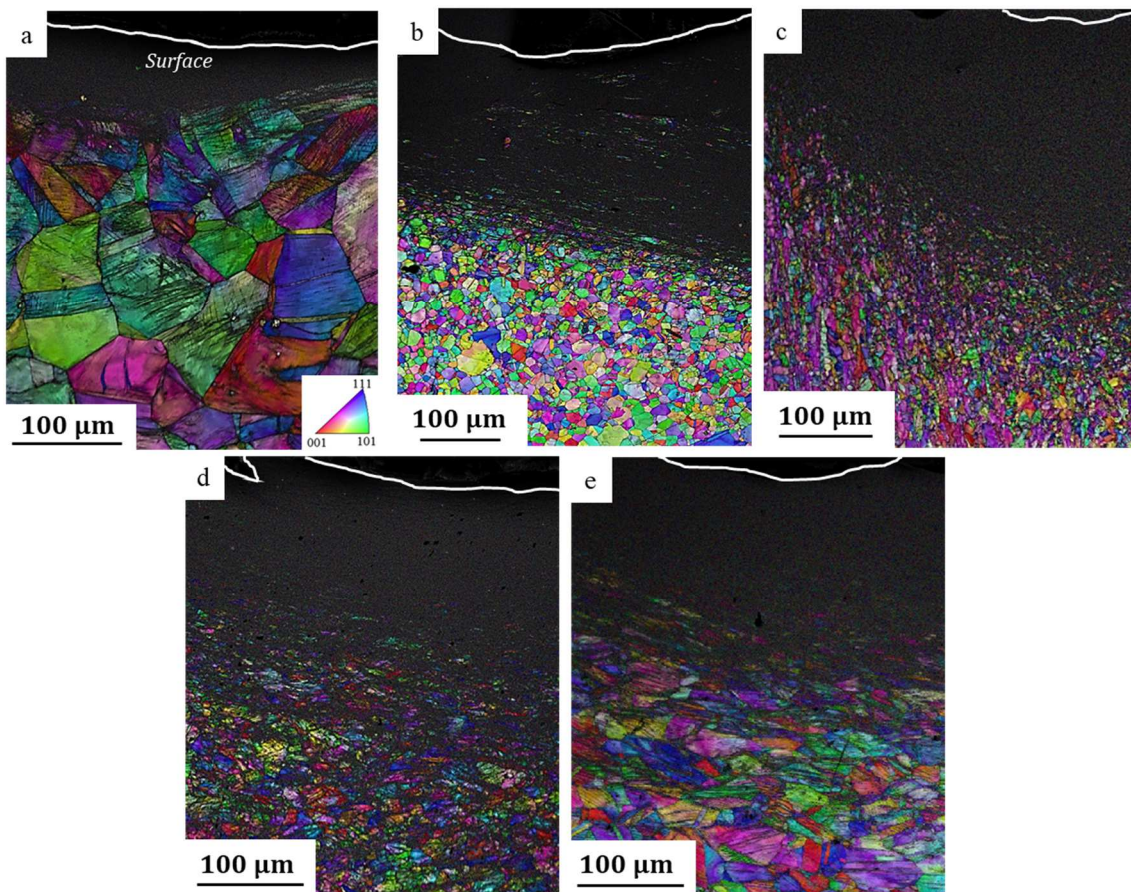
184 Both 316L and 316LN present after galling test at 350 MPa very high Sa values. As opposite,
185 Nitronic60 shows the lowest Sa, while AISI660's and Uranus45N's are intermediary. This is in
186 good agreement with visual inspection and therefore shows that surface degradation due to
187 galling is the most severe for 316L and 316LN. However, when comparing Sa/ ΔP , one can

188 notice comparable values between Nitronic60, AISI660 and Uranus45N, meaning that galling
189 severity is equivalent for these grades for a given pressure difference ΔP .

190 In conclusion, three different wear phenomena, coming with variable galling resistances are
191 observed. These observations suggest the existence of several galling features. In order to
192 confirm this trend, microstructural investigations are performed on galled samples.

193 3.2. Microstructure investigations

194 EBSD analyses are performed on cross section of galled samples after a test realized at 350 MPa
195 in order to characterize microstructure evolution (Figure 8).



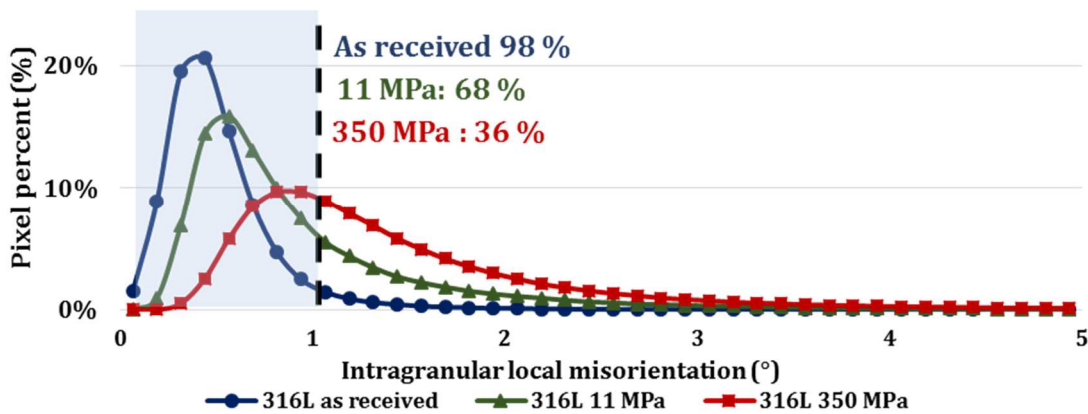
196

197 *Figure 8 : Cross section inverse pole figure (IPF) following [RD] for tested pins after galling test realized at 350*
198 *MPa. White lines represent the contact surface. a- Nitronic60, b- AISI660, c- Uranus45N, d- 316L, e- 316LN*

199 For all grades, a non-indexed region is observed in close surface due to the lattice distortion
200 induced during sollicitation. However, microstructure evolution differs from one grade to

201 another. The microstructure of Nitronic60 is the least modified by galling apparition while 316L
 202 and 316LN show the most deformed microstructure. AISI660, Uranus45N qualitatively present
 203 intermediary microstructural degradation.

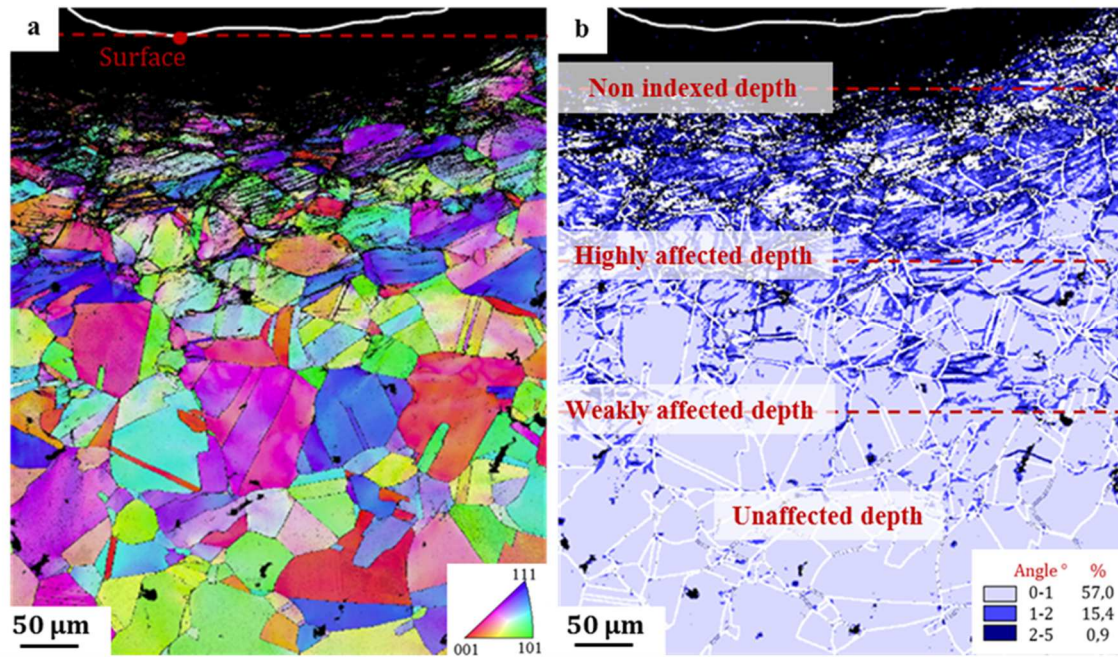
204 In order to quantify microstructure changes observed, local misorientation are measured, as
 205 proposed in several papers [6,7]. After galling occurrence, local intragranular misorientation
 206 rises close to the surface (Figure 9).



207
 208 *Figure 9 : Relative frequency associated with a given local misorientation in the case of 316L as received, after a*
 209 *galling test at 11 MPa and after a galling test at 350 MPa*

210 As seen on Figure 9, at least 96% of the pixel present an intragranular local misorientation
 211 lower than 1° before galling test. Once galling occurred, the percentage of pixel having a
 212 misorientation lower than 1° rapidly falls to 70% to 30% depending on applied pressure. It is
 213 therefore considered that most local misorientation higher than 1° is a result of galling test.
 214 Using this information, one can measure the average intragranular misorientation at a given
 215 depth and determine the depth until which the microstructure is significantly modified by
 216 galling.

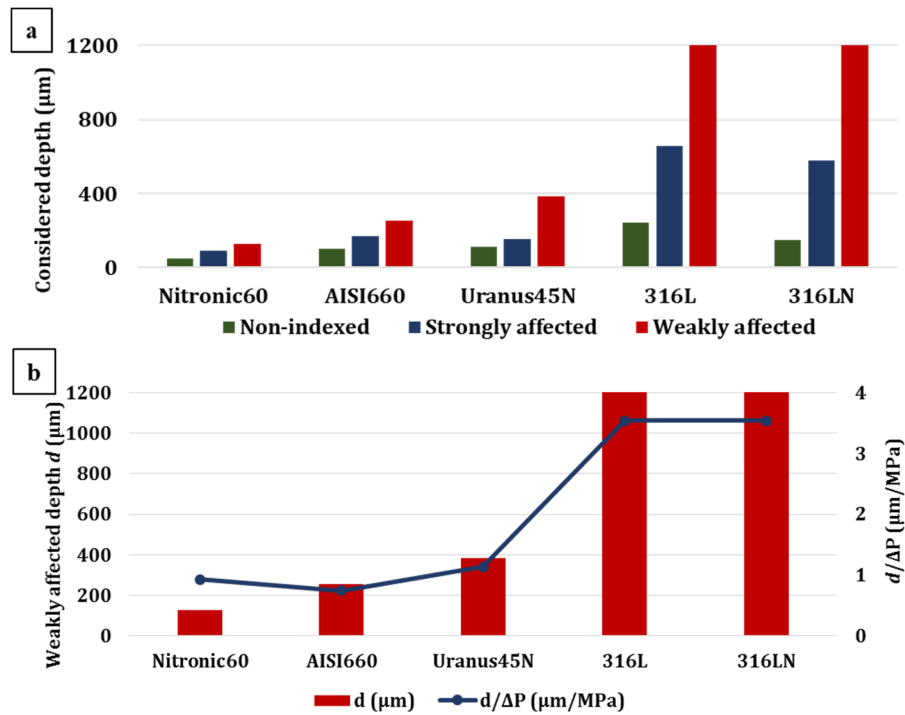
217 Several affected zones are proposed in order to better describe microstructure evolution after
 218 galling test (Figure 10).



219

220 *Figure 10 : a- Inverse pole figure (IPF) of 316L after galling test at 88 MPa and b- corresponding Kernel Average*
 221 *Misorientation (KAM) indicating the local intragranular misorientation*

222 As shown on Figure 10, four zones are used in this work. So-called “non-indexed depth”
 223 corresponds to the depth until more than 70% of pixels can not be indexed by EBSD analysis.
 224 Below this zone, the local misorientation is high, with a “strongly affected depth” indicating
 225 that at least 70% of pixels are either non-indexed or having an intragranular misorientation
 226 higher than 1°. This is followed by a “weakly affected depth” noted d , where 30% to 80% of
 227 pixels have an intragranular misorientation lower than 1°. Finally, the “unaffected depth”
 228 corresponds to the depth from which microstructure is barely affected by galling apparition,
 229 with more than 80% of pixels having a local intragranular misorientation lower than 1°. Figure
 230 11 sums up the different affected depths d for each considered grade as well as $d/\Delta P$.



231

232

233

234

Figure 11: Determination of a- non-indexed depth, strongly affected depth and weakly affected depth d after galling test realized at 350 MPa for each grade. b- weakly affected depth d compared to $d/\Delta P$

235

Nitronic60 presents both the lowest non-indexed depth, strongly affected depth and weakly

236

affected depth. As opposite, 316L and 316LN both show huge affected depths, with a weakly

237

affected depth higher than 1200 μm , which is the maximum depth investigated. AISI660 and

238

Uranus45N exhibit intermediary values. Once again, when comparing reduced depths, one can

239

notice that Nitronic60, AISI660 and Uranus45N all present equivalent reduced $d/\Delta P$ values.

240

These observations are in good agreement with surface investigations previously discussed.

241

3.3. Identified galling categories

242

We can conclude from previous investigations that Nitronic60 presents both the lowest surface

243

modification and the slightest microstructural modification, coming with unique wear

244

mechanism. AISI660 and Uranus45 are mainly worn by adhesive wear, leading to a relatively

245

weak surface and microstructure modifications. Finally, 316L and 316LN show similar

246

tendencies, with a mainly abrasive wear and important surface and microstructure

247

modifications. Consequently, three galling categories are proposed herein.

- 248 • **Tolerant galling** (Nitronic60) can be described as the category having the highest galling
249 resistance. Galling threshold is high and galling severity is low. Galled samples exhibit a
250 surface state presenting tiny adhesive wear spots, located homogeneously on the pin
251 surface. The in-depth microstructure is also weakly affected.
- 252 • **Moderate galling** (AISI660 and Uranus45N) presents mainly adhesive wear, initiated at
253 first at the periphery of the pin. Galling threshold is low but galling severity is low as well.
254 Very few abrasive wear is observed. Both $Sa/\Delta P$ and $d/\Delta P$ of same order of magnitude as
255 for Nitronic60.
- 256 • **Severe galling** (316L, 316LN) is the most destructive category and characterized by
257 abrasive wear by third body generation and smearing appearing even at low pressure.
258 Sample surface are heavily deformed, and microstructure is affected for the most important
259 depth. Galling threshold is low and galling severity is high.

260 4. Discussion on galling categories origins

261 In order to have insights into the origins of these galling categories, several microstructural
262 investigations have been performed. Two main points stands out of these investigations: phase
263 transformation and nanostructuring in close surface.

264 4.1. Phase transformations

265 Austenite is metastable and subject to phase transformation when applied thermal or mechanical
266 solicitation. In our test configuration, thermal aspects are neglected due to the localization of
267 heat input in extreme surface. However, depending on the Stacking Fault Energy (SFE), the
268 strain applied onto the samples might transform austenite into Strain Induced Martensite (SIM).

269 SFE is the energy possessed by a structure due to the discontinuity in the stacking planes or
270 closed-pack plane leading to partial dislocations in FCC [14]. SFE strongly affects deformation
271 mechanisms as well as phase transformation during solicitation of a given material [12,25,26].

272 For low SFE values, typically $SFE \leq 20 \text{ mJ.m}^{-2}$ [27], phase transformation is likely to happen.

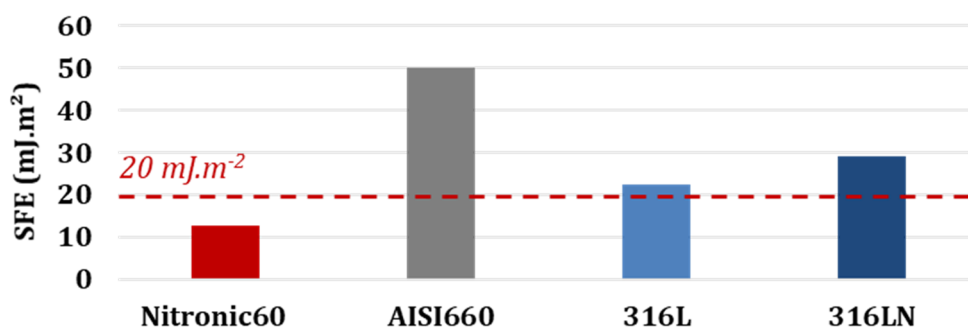
273 This transformation can lead to either α' martensite (pseudo-cubic body centered) or ϵ

274 martensite (hexagonal compact) [27,28]. Two transformation sequences are commonly found in
 275 the literature: $\gamma \rightarrow \varepsilon \rightarrow \alpha'$ and $\gamma \rightarrow \alpha'$ [29,30]. In the first sequence, ε can act as nucleation sites
 276 for the formation of α' while in the second one α' directly forms from austenite γ . However, if
 277 only a small amount of strain is provided to the system, the first transformation sequence is
 278 stopped and no α' martensite is observed. Thus, depending on the chemical composition and
 279 strain history, both α' and ε martensite can be observed. Several strain responses can result from
 280 the competition between these phases [31–33] and galling tendency is susceptible to be affected
 281 [34].

282 SFE can be calculated using various methods, including *ab initio* approach [35,36],
 283 thermodynamic modelling [37,38], experimental measurements [29,39,40] or approximate
 284 models for SFE estimations [41,42]. In this study, the objective is to estimate SFE in order to
 285 determine if phase transformation is likely to occur or not. Thus, approximate models are
 286 selected instead of more accurate but more complex methodologies. Meric de Bellefon *et al.*
 287 [26] (equation 1) proposed one of the most convincing model for austenitic steels, with a good
 288 agreement with experimental results, leading to Figure 12 for selected grades.

$$SFE (mJ.m^{-2}) = 2.2 + 40 * \%C - 3.6 * \%N - 0.016 * \%Cr + 1.9 * \%Ni - 2.9 * \%Si + 0.5 * \%Mn + 0.77 * \%Mo \quad (1)$$

289



290

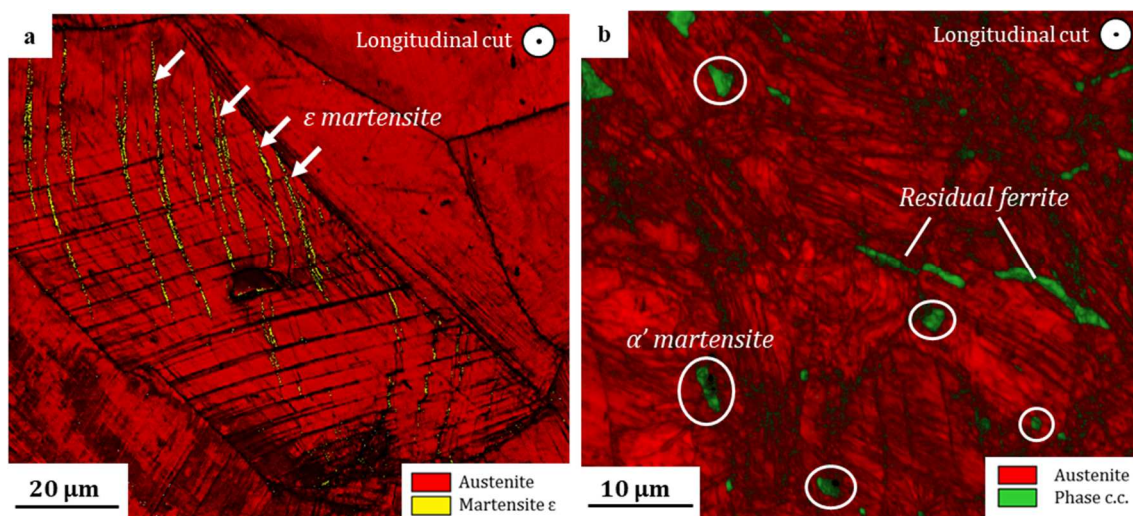
291 *Figure 12 : Estimated SFE for austenitic stainless steels using Meric de Bellefon et al. equation. The dashed line 20*
 292 *mJ.m⁻² correspond to the value where phase transformation is likely to be found*

293 Following this equation, Nitronic60 is the most susceptible to form SIM, while AISI660 is not
 294 assumed to present any phase transformation.

295 Rogers *et al* [43] showed that austenite transforms into an α' pseudo-cubic martensite for galled
296 samples of 316L stainless steel. However, no data could be found in the literature concerning
297 the martensite transformation of other stainless steel grades during galling test.

298 In order to study the transformed phases, EBSD analyses are performed on galled samples of
299 each austenitic grades. From now on, results are shown for one grade of each galling category:
300 Nitronic60 (tolerant galling), AISI660 (moderate galling) and 316L (severe galling), which
301 present the most representative case.

302 For Nitronic60 (Figure 13.a), ϵ martensite is visible in thin laths. No evidence of α' martensite
303 has been found for this grade. As opposite, α' martensite is observed with a pseudo-spherical
304 shape for 316L (Figure 13.b) while no ϵ martensite could be found. No martensitic
305 transformation has been observed for AISI660 using EBSD analysis.



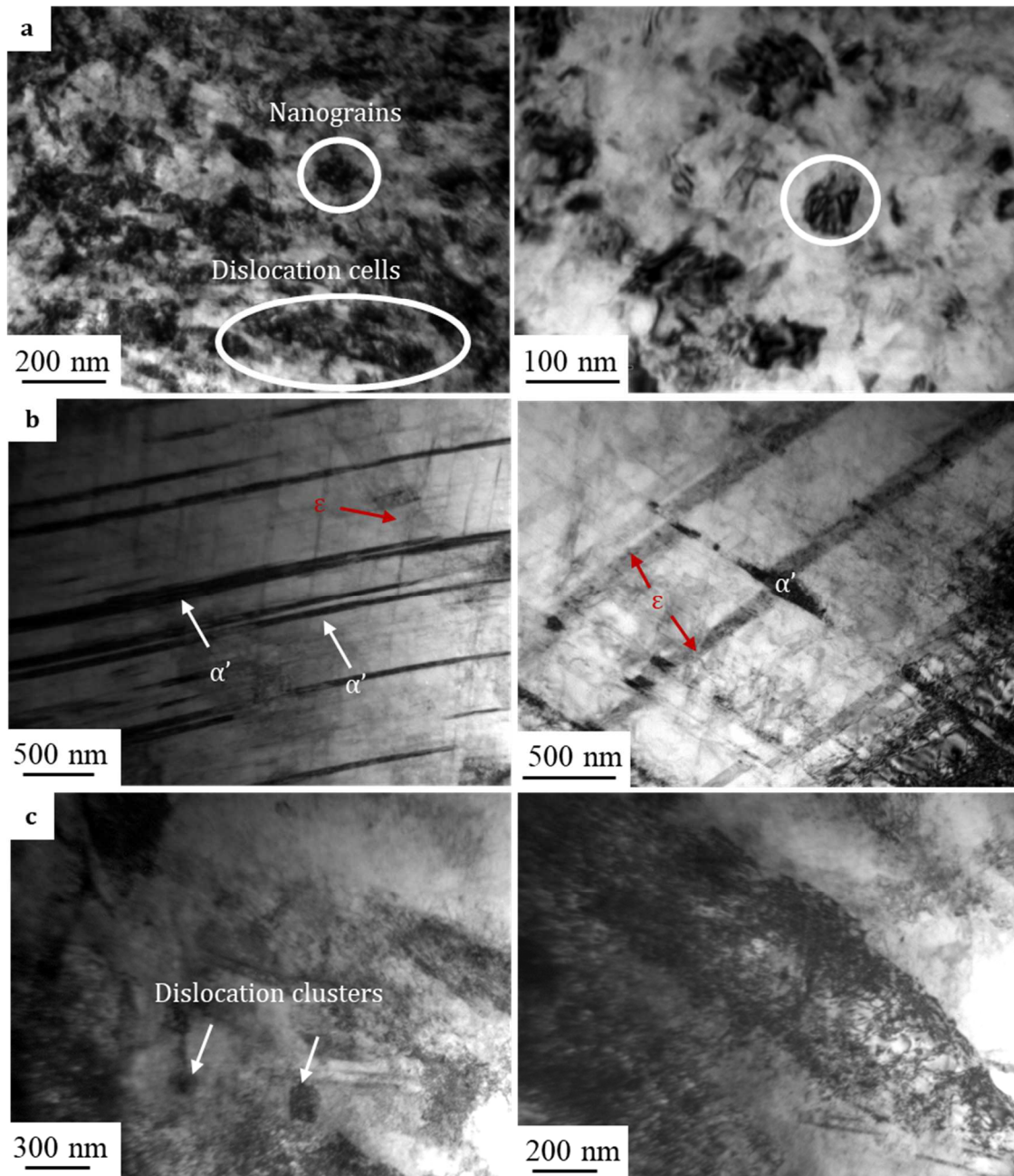
306
307 *Figure 13 : Formation after a galling test realized at 350 μm of a- ϵ martensite inside Nitronic60 (400 μm depth) and*
308 *b- pseudo-cubic α' martensite inside 316L (550 μm depth)*

309 It can be concluded that for Nitronic60 (tolerant galling), austenite is transformed into
310 hexagonal compact martensite, while 316L and 316LN (severe galling) form pseudo-cubic body
311 centered martensite. AISI660 (moderate galling) does not show any evidence of phase
312 transformation at this scale.

313 ϵ hexagonal compact martensite is most probably beneficial to galling resistance while α'
314 pseudo-cubic body centered martensite might be detrimental [34]. Even if the mechanisms are
315 still unclear, one explanation would be to consider the low number of slip systems in hexagonal
316 compact phase compared to those of body centered phase. Lowering the ease of cross-slip
317 hinders plastic strain diffusion and therefore lowers galling severity [12,44,45]. Therefore,
318 lowering the amount of slip systems for a given configuration could be a way to limit cross-slip
319 and improve galling resistance. Furthermore, the elongated shape of ϵ martensite as compared to
320 the almost spherical α' makes it more prone to hinder dislocation motion, thus confining
321 dislocations in close surface.

322 4.2. TEM investigations

323 Finally, TEM investigations have been performed in order to examine the evolution of
324 microstructure in close surface after a galling test realized at 350 MPa.



325

326 *Figure 14 : TEM investigations realized in extreme surface at one of the sample's valley after a galling test realized*

327 *at 350 MPa. a- Formation of dislocations cells and nanograins for Nitronic60, b- Martensite laths consisting of*

328 *mainly α' martensite and a few ϵ laths in AISI660 c- Statistically distributed dislocations and dislocation clusters in*

329

316L

330 Figure 14 shows three distinct microstructures in extreme surface depending on galling

331 category. For Nitronic60, dislocation cells and nanograins of size ranging from 30 nm to 50 nm

332 are observed. This indicates a high capacity of microstructural reorganization for this grade.

333 Moreover, the low depth of affected microstructure pointed out earlier could be explained by the

334 localization of dislocations inside these nanograins. For AISI660, thin laths of both α'
335 martensite and ϵ martensite are observed. These films could not be observed by EBSD
336 investigation, which suggests that this SIM is only localized at the extreme surface of the
337 sample. The coexistence in extreme surface of both α' and ϵ martensite reinforces the
338 conclusions drawn in part 4.1 and suggests that the intermediary galling resistance of this grade
339 could originate in this dual phase transformation. For 316L, no microstructural reorganization is
340 found, with statistically distributed dislocations and a few dislocation clusters around the
341 sample. Dislocations are therefore free to migrate to the core material, which may explain the
342 higher affected depth for this grade.

343 As a result, it is proposed that both ϵ martensite formation and nanograins formation are
344 beneficial for galling resistance. These differences in phase transformation and microstructure in
345 the extreme surface may explain the differences in galling categories.

346 5. Conclusion

347 This paper aims at better describing galling phenomena and understanding the consequences of
348 galling apparition. Once galling occurred, several wear mechanisms can be seen depending on
349 selected grade, leading to variable severity of galling. Macroscopic and microscopic
350 investigations (3D profilometry, SEM, EBSD, TEM) performed on five stainless steels allowed
351 us to distinguish three distinct galling mechanisms.

- 352 • Tolerant galling appears in the form of adhesive wear spots homogeneously located on
353 sample surface. Both surface degradation and in-depth microstructure evolution the
354 weakest among all the galling categories. Galling threshold is high and galling severity is
355 low.
- 356 • Moderate galling presents adhesive wear located solely on pin periphery at low pressure.
357 The weakly affected depth divided by excessive pressure $d/\Delta P$ as well as $Sa/\Delta P$ are of
358 same order as Nitronic60. Both galling threshold and galling severity are low.

359 • Severe galling is the most destructive type of galling, characterized by a heavily damaged
360 surface, with high amount of third bodies as well as a deeply modified microstructure.
361 Wear is mainly abrasive with an important smearing on the surface. Material transfer, when
362 occurring, is a consequence of third body generation and abrasive wear. Galling threshold
363 is low and galling severity is high.

364 The origins of the identified galling categories have then been discussed. It appears that for each
365 galling category, different phase transformations can be observed. The transformation from
366 austenite to Strain Induced Martensite (SIM), can be either pseudo-body centered (α') or
367 hexagonal compact (ϵ). Nitronic60 presents hexagonal compact martensite ϵ , as opposite to the
368 α' martensite observed in 316L. Moderate galling AISI660 presents both α' and ϵ martensite in
369 extreme surface. The c/a ratio is higher for ϵ (hcp) martensite as compared to the quasi-cubic α'
370 martensite, thus, the galling resistance is increased [14].

371 The formation of nanograins, as seen in Nitronic60 is also suspected to be beneficial to the
372 galling resistance. As opposite, the lack of reorganization in 316L could explain the elevated
373 depth of affected microstructure.

374 In regards with presented results, the authors recommend to further investigate on the relation
375 between dislocation mobility and galling resistance. Indeed, nanograin formation and hexagonal
376 compact phase transformation, observed for Nitronic60, could be ways to lower the mobility of
377 dislocations and may explain the higher galling resistance of this grade.

378

379 ***Acknowledgement***

380 The authors would like to thank the Hauts-de-France Region and the European Regional
381 Development Fund (ERDF) 2014/2020 for the funding of this work. The authors would also like
382 to thank David CAZE (CETIM Senlis) for galling test realization. Special thanks go to Abdelali
383 OUDRISS and Xavier FEAUGAS from Université de La Rochelle for TEM investigations and
384 exploitation.

385 ***References***

- 386 [1] R. Badji, T. Chauveau, B. Bacroix, Texture, misorientation and mechanical anisotropy in a
387 deformed dual phase stainless steel weld joint, *Mater. Sci. Eng. A.* 575 (2013) 94–103.
388 <https://doi.org/10.1016/j.msea.2013.03.018>.
- 389 [2] C. Herve, P. Friedrich, Y.-M. Chen, D. Caze, Galling detection by acoustic emission
390 according to ASTM G98, (n.d.).
- 391 [3] J. Vikström, Galling resistance of hardfacing alloys replacing Stellite, *Wear.* 179 (1994)
392 143–146. [https://doi.org/10.1016/0043-1648\(94\)90232-1](https://doi.org/10.1016/0043-1648(94)90232-1).
- 393 [4] B. Podgornik, S. Hogmark, Surface modification to improve friction and galling properties
394 of forming tools, *J. Mater. Process. Technol.* 174 (2006) 334–341.
395 <https://doi.org/10.1016/j.jmatprotec.2006.01.016>.
- 396 [5] P. Karlsson, A. Gård, P. Krakhmalev, J. Bergström, Galling resistance and wear
397 mechanisms for cold-work tool steels in lubricated sliding against high strength stainless
398 steel sheets, *Wear.* 286–287 (2012) 92–97. <https://doi.org/10.1016/j.wear.2011.04.002>.
- 399 [6] R. Unnikrishnan, S.M. Northover, H. Jazaeri, P.J. Bouchard, Investigating plastic
400 deformation around a reheat-crack in a 316H austenitic stainless steel weldment by
401 misorientation mapping, *Procedia Struct. Integr.* 2 (2016) 3501–3507.
402 <https://doi.org/10.1016/j.prostr.2016.06.436>.
- 403 [7] B. Dylewski, M. Risbet, S. Bouvier, The tridimensional gradient of microstructure in worn
404 rails – Experimental characterization of plastic deformation accumulated by RCF, *Wear.*
405 392–393 (2017) 50–59. <https://doi.org/10.1016/j.wear.2017.09.001>.
- 406 [8] A. Gård, P. Krakhmalev, J. Bergström, Influence of tool steel microstructure on origin of
407 galling initiation and wear mechanisms under dry sliding against a carbon steel sheet,
408 *Wear.* 267 (2009) 387–393. <https://doi.org/10.1016/j.wear.2008.11.013>.
- 409 [9] J. Marteau, Caractérisation multi-échelle et analyse par essai d'indentation instrumentée
410 de matériaux à gradient générés par procédés mécaniques et thermo-chimiques de
411 traitement de surface, PhD Thesis, Université de Technologie de Compiègne, France,
412 2013. <https://tel.archives-ouvertes.fr/tel-00937956/> (accessed December 21, 2015).
- 413 [10] G. Maistro, C. Oikonomou, L. Rogström, L. Nyborg, Y. Cao, Understanding the
414 microstructure-properties relationship of low-temperature carburized austenitic stainless
415 steels through EBSD analysis, *Surf. Coat. Technol.* 322 (2017) 141–151.
416 <https://doi.org/10.1016/j.surfcoat.2017.05.036>.
- 417 [11] J.P. Hirth, D.A. Rigney, Crystal plasticity and the delamination theory of wear, *Wear.* 39
418 (1976) 133–141. [https://doi.org/10.1016/0043-1648\(76\)90229-5](https://doi.org/10.1016/0043-1648(76)90229-5).
- 419 [12] K.J. Bhansali, A.E. Miller, The role of stacking fault energy on galling and wear behavior,
420 *Wear.* 75 (1982) 241–252. [https://doi.org/10.1016/0043-1648\(82\)90151-X](https://doi.org/10.1016/0043-1648(82)90151-X).
- 421 [13] R. Smith, M. Doran, D. Gandy, S. Babu, L. Wu, A.J. Ramirez, P.M. Anderson,
422 Development of a gall-resistant stainless-steel hardfacing alloy, *Mater. Des.* (n.d.).
423 <https://doi.org/10.1016/j.matdes.2018.01.020>.
- 424 [14] K.K. Kakulite, B. Kandasubramanian, Rudiment of ‘galling: Tribological phenomenon’
425 for engineering components in aggregate with the advancement in functioning of the anti-
426 galling coatings, *Surf. Interfaces.* 17 (2019) 100383.
427 <https://doi.org/10.1016/j.surfin.2019.100383>.
- 428 [15] I. Heikkilä, L. Slycke, Influence of nitrogen alloying on galling properties of pm tool
429 steels, (n.d.).
- 430 [16] T. Arai, Y. Tsuchiya, Role of carbide and nitride in antigalling property, *Met. Transf.*
431 *Galling Met. Syst.* (1986) 198–216.
- 432 [17] D.-C. Ko, S.-G. Kim, B.-M. Kim, Influence of microstructure on galling resistance of
433 cold-work tool steels with different chemical compositions when sliding against ultra-
434 high-strength steel sheets under dry condition, *Wear.* 338–339 (2015) 362–371.
435 <https://doi.org/10.1016/j.wear.2015.07.014>.
- 436 [18] S.C. Agarwal, H. Ocken, The microstructure and galling wear of a laser-melted cobalt-
437 base hardfacing alloy, *Wear.* 140 (1990) 223–233. [https://doi.org/10.1016/0043-1648\(90\)90085-O](https://doi.org/10.1016/0043-1648(90)90085-O).
- 438
439 [19] H. Ocken, The galling wear resistance of new iron-base hardfacing alloys: a comparison
440 with established cobalt- and nickel-base alloys, *Surf. Coat. Technol.* (1995) 456–461.

- 441 [20] K.C. Anthony, Wear-resistant cobalt-free alloys, *J. Mechanical Eng. Technol.* 35 (1983)
442 52–60.
- 443 [21] B.M. Voss, M.P. Pereira, B.F. Rolfe, M.C. Doolan, A new methodology for measuring
444 galling wear severity in high strength steels, *Wear.* 390–391 (2017) 334–345.
445 <https://doi.org/10.1016/j.wear.2017.09.002>.
- 446 [22] S.R. Hummel, Development of a galling resistance test method with a uniform stress
447 distribution, *Tribol. Int.* 41 (2008) 175–180. <https://doi.org/10.1016/j.triboint.2007.07.009>.
- 448 [23] J.A. Siefert, S.S. Babu, Experimental observations of wear in specimens tested to ASTM
449 G98, *Wear.* 320 (2014) 111–119. <https://doi.org/10.1016/j.wear.2014.08.017>.
- 450 [24] A. Saidoun, C. Herve, Y.M. Chen, T. Lesage, S. Bouvier, Galling detection by acoustic
451 emission (AE) according to ASTM G98, in: 2018.
- 452 [25] D. Arpan, Revisiting stacking fault energy of steels, *Metall. Mater. Trans. A.* (2015).
453 <https://doi.org/10.1007/s11661-015-3266-9>.
- 454 [26] G. Meric de Bellefon, J.C. van Duysen, K. Sridharan, Composition-dependence of
455 stacking fault energy in austenitic stainless steels through linear regression with random
456 intercepts, *J. Nucl. Mater.* 492 (2017) 227–230.
457 <https://doi.org/10.1016/j.jnucmat.2017.05.037>.
- 458 [27] O. Grässel, G. Frommeyer, C. Derder, H. Hofmann, Phase Transformations and
459 Mechanical Properties of Fe-Mn-Si-AlTRIP-Steels, *J. Phys. IV.* 07 (1997) C5-383-C5-
460 388. <https://doi.org/10.1051/jp4:1997560>.
- 461 [28] A. Saeed-Akbari, J. Imlau, U. Prah, W. Bleck, Derivation and Variation in Composition-
462 Dependent Stacking Fault Energy Maps Based on Subregular Solution Model in High-
463 Manganese Steels, *Metall. Mater. Trans. A.* 40 (2009) 3076–3090.
464 <https://doi.org/10.1007/s11661-009-0050-8>.
- 465 [29] D.T. Pierce, J.A. Jiménez, J. Bentley, D. Raabe, J.E. Wittig, The influence of stacking
466 fault energy on the microstructural and strain-hardening evolution of Fe–Mn–Al–Si steels
467 during tensile deformation, *Acta Mater.* 100 (2015) 178–190.
468 <https://doi.org/10.1016/j.actamat.2015.08.030>.
- 469 [30] Y. Li, W. Li, N. Min, W. Liu, C. Zhang, X. Jin, Mechanical response of a medium
470 manganese steel with encapsulated austenite, *Scr. Mater.* 178 (2020) 211–217.
471 <https://doi.org/10.1016/j.scriptamat.2019.11.033>.
- 472 [31] K. Spencer, M. Véron, K. Yu-Zhang, J.D. Embury, The strain induced martensite
473 transformation in austenitic stainless steels: Part 1 – Influence of temperature and strain
474 history, *Mater. Sci. Technol.* 25 (2009) 7–17. <https://doi.org/10.1179/174328408X293603>.
- 475 [32] Q.X. Dai, X.N. Cheng, X.M. Luo, Y.T. Zhao, Structural parameters of the martensite
476 transformation for austenitic steels, *Mater. Charact.* 49 (2002) 367–371.
477 [https://doi.org/10.1016/S1044-5803\(03\)00035-4](https://doi.org/10.1016/S1044-5803(03)00035-4).
- 478 [33] W. Pachla, J. Skiba, M. Kulczyk, S. Przybysz, M. Przybysz, M. Wróblewska, R.
479 Diduszko, R. Stępnia, J. Bajorek, M. Radomski, W. Fąfara, Nanostructurization of 316L
480 type austenitic stainless steels by hydrostatic extrusion, *Mater. Sci. Eng. A.* 615 (2014)
481 116–127. <https://doi.org/10.1016/j.msea.2014.07.069>.
- 482 [34] K.-L. Hsu, T.M. Ahn, D.A. Rigney, Friction, wear and microstructure of unlubricated
483 austenitic stainless steels, *Wear.* 60 (1980) 13–37. [https://doi.org/10.1016/0043-1648\(80\)90247-1](https://doi.org/10.1016/0043-1648(80)90247-1).
- 485 [35] T.L. Achmad, W. Fu, H. Chen, C. Zhang, Z.-G. Yang, First-principles calculations of
486 generalized-stacking-fault-energy of Co-based alloys, *Comput. Mater. Sci.* 121 (2016) 86–
487 96. <https://doi.org/10.1016/j.commatsci.2016.04.031>.
- 488 [36] K.R. Limmer, J.E. Medvedeva, D.C.V. Aken, N.I. Medvedeva, Ab initio simulation of
489 alloying effect on stacking fault energy in fcc Fe, *Comput. Mater. Sci.* 99 (2015) 253–255.
490 <https://doi.org/10.1016/j.commatsci.2014.12.015>.
- 491 [37] S. Curtze, V.-T. Kuokkala, A. Oikari, J. Talonen, H. Hänninen, Thermodynamic modeling
492 of the stacking fault energy of austenitic steels, *Acta Mater.* 59 (2011) 1068–1076.
493 <https://doi.org/10.1016/j.actamat.2010.10.037>.

- 494 [38] R. Li, S. Lu, D. Kim, S. Schönecker, J. Zhao, S.K. Kwon, L. Vitos, Stacking fault energy
495 of face-centered cubic metals: thermodynamic and ab initio approaches, *J. Phys. Condens.*
496 *Matter.* 28 (2016) 395001. <https://doi.org/10.1088/0953-8984/28/39/395001>.
- 497 [39] W. Reick, M. Pohl, A. Padilha, Determination of stacking fault energy of austenite in a
498 duplex stainless steel, *Steel Res.* 67 (1996) 253–256.
499 <https://doi.org/10.1002/srin.199605486>.
- 500 [40] D.T. Pierce, J.A. Jiménez, J. Bentley, D. Raabe, C. Oskay, J.E. Wittig, The influence of
501 manganese content on the stacking fault and austenite/ ϵ -martensite interfacial energies in
502 Fe–Mn–(Al–Si) steels investigated by experiment and theory, *Acta Mater.* 68 (2014) 238–
503 253. <https://doi.org/10.1016/j.actamat.2014.01.001>.
- 504 [41] R.E. Schramm, R.P. Reed, Stacking fault energies of seven commercial austenitic stainless
505 steels, *Metall. Trans. A.* 6 (1975) 1345–1351. <https://doi.org/10.1007/BF02641927>.
- 506 [42] T. Yonezawa, K. Suzuki, S. Ooki, A. Hashimoto, The Effect of Chemical Composition
507 and Heat Treatment Conditions on Stacking Fault Energy for Fe–Cr–Ni Austenitic
508 Stainless Steel, *Metall. Mater. Trans. A.* 44 (2013) 5884–5896.
509 <https://doi.org/10.1007/s11661-013-1943-0>.
- 510 [43] S.R. Rogers, D. Bowden, R. Unnikrishnan, F. Scenini, M. Preuss, D. Stewart, D. Dini, D.
511 Dye, The interaction of galling and oxidation in 316L stainless steel, *Wear.* 450–451
512 (2020) 203234. <https://doi.org/10.1016/j.wear.2020.203234>.
- 513 [44] D.H. Buckley, *Surface effects in adhesion, friction, wear, and lubrication*, 1981.
514 [https://www.elsevier.com/books/surface-effects-in-adhesion-friction-wear-and-](https://www.elsevier.com/books/surface-effects-in-adhesion-friction-wear-and-lubrication/buckley/978-0-444-41966-8)
515 [lubrication/buckley/978-0-444-41966-8](https://www.elsevier.com/books/surface-effects-in-adhesion-friction-wear-and-lubrication/buckley/978-0-444-41966-8) (accessed August 20, 2018).
- 516 [45] D.H. Buckley, The Influence of the Atomic Nature of Crystalline Materials on Friction, *E*
517 *Trans.* 11 (1968) 89–100. <https://doi.org/10.1080/05698196808972212>.